Shear debonding at concrete repair interfaces: An integrated experimental and numerical study

Case Studies in Construction Materials 24 (2026) e06160

Contents lists available at ScienceDirect

Case Studies in Construction Materials

journal homepage: www.elsevier.com/locate/cscm

Shear debonding at concrete repair interfaces: An integrated experimental and numerical study

Vahid Shafaie [a], Oveys Ghodousian [b], Marco Domaneschi [c], Majid Movahedi Rad [a,*]

[a] Department of Structural and Geotechnical Engineering, Széchenyi István University, Győr 9026, Hungary
[b] Department of Engineering, Tak. C., Islamic Azad University, Takestan, Iran
[c] Department of Structural, Geotechnical and Building Engineering, Politecnico di Torino, Corso Duca degli Abruzzi, 24, Turin 10129, Italy

ARTICLE INFO

Keywords:
Shear Bond
Concrete Repair
Interface Behavior
Finite Element Modeling
Concrete Damaged Plasticity
Element Deletion

ABSTRACT

Durable repair of concrete structures relies critically on the shear bond between new and existing concrete, yet reliable prediction of this bond remains challenging due to highly localized interfacial damage mechanisms. Conventional numerical interaction strategies, such as tie constraints, are unable to capture progressive debonding, often leading to unconservative estimates of load transfer and structural capacity. This study presents a three-dimensional Finite Element approach that explicitly represents the repair interface through thin sacrificial layers governed by Concrete Damaged Plasticity and element deletion. The approach is validated against a dedicated shear push-out experimental campaign in which the cement content of the repair layer was systematically varied from 300 to 550 kg/m^3 while all other parameters are held constant. The numerical model accurately reproduces the experimentally observed zipper-type interfacial debonding and captures both the onset and propagation of localized shear damage, with satisfactory quantitative agreement. Building on this validation, continuous calibration curves are derived with high statistical correlation ($R^2 \approx 0.95$) and low predictive error (NRMSE $< 9\%$), directly relating repair cement content to shear bond strength and interface compressive strength. Specifically, the framework captures the nonlinear increase in shear bond strength from 0.21 to 1.85 MPa. The proposed method provides a physically grounded and design-oriented bridge between mix proportioning and structural simulation, enabling consistent definition of interface parameters without iterative numerical tuning.

1. Introduction

The structural rehabilitation of aging civil infrastructure is a critical priority for the construction industry, requiring repair strategies that restore load-bearing capacity and extend service life by forming durable composite systems. In applications ranging from pavement screeds to structural overlays, the efficacy of the repair depends on achieving monolithic action between the existing substrate and the new repair layer [1–3]. However, the interface between the mature substrate and the fresh overlay constitutes a zone of mechanical and thermodynamic discontinuity, commonly referred to as the Interfacial Transition Zone (ITZ), which typically exhibits higher porosity and micro-cracking compared to the bulk material [4]. Premature loss of adhesion within this weak link can

* Corresponding author.
E-mail address: majidmr@sze.hu (M. Movahedi Rad).

https://doi.org/10.1016/j.cscm.2026.e06160
Received 11 February 2026; Received in revised form 31 March 2026; Accepted 18 May 2026
Available online 19 May 2026

trigger delamination, compromise serviceability, or precipitate catastrophic structural failure [5,6].

Experimental investigations have demonstrated that the quality of this interfacial bond is governed by a complex interaction of factors, including substrate surface roughness and moisture condition, curing regimes, and critically, the mechanical properties and composition of the repair material [7–11]. While advanced alternatives such as polymer-modified mortars or fiber-reinforced composites offer enhanced ductility [9,12–14], conventional cement-based concrete remains the predominant choice for general repairs due to its physico-chemical compatibility with existing concrete, thermal stability, and economic viability [15–17]. Nevertheless, improper mixture proportioning, specifically with regard to cement content, frequently leads to debonding issues under environmental and mechanical loading [18]. Recent studies have also further highlighted the bonding behavior between new and old concrete and confirmed the importance of interface-related material factors in governing composite performance [19]. Recent review studies have further emphasized that interface condition, material mismatch, curing, and overlay composition remain among the dominant variables controlling the mechanical performance of concrete-to-concrete composites [19,20]. Consequently, establishing robust methodologies to quantify shear bond capacity, while explicitly accounting for mix design variations, is a prerequisite for the rational design of resilient repair systems.

Quantifying the mechanical integrity of the repair-substrate interface relies on established experimental protocols, yet identifying a method that accurately reflects in-situ stress states remains a subject of debate [15]. While tensile pull-off tests are widely standardized for assessing adhesion, they frequently fail to capture the shear-dominated forces that typically drive delamination in structural overlays [21]. Similarly, although slant-shear tests are frequently employed, rigorous comparative studies indicate that the compressive strut action inherent in the specimen geometry can inflate apparent strengths that do not reflect true interfacial cohesion [12,22]. Research indicates that this superimposition of normal compression artificially enhances apparent bond capacity by frictional interlock, underscoring the necessity for test configurations that minimize such interference in order to obtain conservative and representative design values [15,23]. Consequently, shear-splitting or *push-out* tests have gained prominence, as they effectively isolate the interface and provoke failure strictly along the bond plane [12,21,22,24]. This broader concern regarding test-method dependency has also been highlighted in comparative studies showing that different bond tests may produce substantially different strength levels for the same repair system, depending on the stress state imposed at the interface [15,25].

Recent investigations have successfully utilized this configuration to calibrate micro-structural bond parameters and predictive frameworks, explicitly highlighting the role of frictional effects in model validation [26,27]. Furthermore, parallel studies on complex composites have further validated the suitability of this method for integration with advanced data-driven optimization frameworks [13,22,24]. At the same time, more recent concrete-to-concrete shear studies have shown that direct or push-off type configurations can provide design-relevant information in terms of cohesion, friction, fracture energy, and failure-mode transition, particularly when surface effects are carefully controlled [28,29]. However, despite this experimental progress, most research campaigns still treat the relationship between mix design variables, interfacial properties, and structural response in an empirical manner. In other words, they identify which parameters influence bond behavior, but they do not explicitly translate these measurable material and mixture variables into the constitutive quantities required for design-oriented numerical models. This unresolved translation from experimentally measurable mix design to FE-ready interface parameters constitutes the central gap addressed in the present study.

This gap becomes even more evident from the numerical modeling perspective. Accurately representing the non-linear behavior of concrete-concrete interfaces in Finite Element (FE) models remains challenging. In practical applications, simplified tie constraints are often adopted to enforce perfect kinematic compatibility between the substrate and the repair layer; however, this assumption suppresses relative slip and prevents the simulation of progressive debonding, leading to systematic overestimation of load transfer and structural capacity [8,30]. To overcome these limitations, cohesive zone models and contact-based formulations have been proposed to describe interface fracture through traction separation laws [31,32]. While these approaches offer improved physical realism compared to rigid constraints, they introduce significant model complexity and require extensive calibration of fracture energy parameters that are often difficult to determine experimentally for heterogeneous cementitious repair systems [33]. Recent FE studies on concrete–concrete composite interfaces have confirmed the usefulness of cohesive formulations, but they have also shown that such approaches typically require calibration from prior experimental or analytical identification procedures rather than from directly usable mix-design variables [34]. As a result, previous numerical frameworks have generally remained case-specific, and the constitutive interface parameters employed in them are not readily transferable to repair mixtures defined at the proportioning stage.

Among the alternative numerical strategies proposed to overcome these limitations, recent studies have successfully employed sacrificial interface layers combined with damage plasticity formulations and element deletion techniques to simulate crack initiation and propagation in bonded systems. In particular, a thin sacrificial adhesive band governed by physically motivated failure criteria has been shown to accurately reproduce shear debonding mechanisms and match experimental splitting shear responses in stone-clad façade systems [35]. These developments demonstrate the potential of sacrificial-interface strategies for reproducing progressive debonding in bonded systems. However, the previously reported applications were developed for materially different composite configurations, such as stone-cladding systems involving concrete substrate, adhesive mortar, and stone layers, rather than concrete repair systems composed of substrate–repair concrete–substrate assemblages. Despite these advances, a critical gap remains for concrete repair interfaces. Although experimental investigations have clearly demonstrated the strong influence of repair mix composition, and specifically cement content, on shear bond performance [7,8,15,21], these empirical relationships have not yet been translated into calibration tools suitable for advanced FE modeling of repair interfaces.

To address this unresolved gap, the present study proposes a unified experimental and numerical framework that directly links repair mix design to the constitutive parameters governing interface failure. A robust three-dimensional FE strategy based on Concrete Damaged Plasticity (CDP) and sacrificial interface layers with element deletion is validated against shear push-out tests on repair concretes with varying cement contents, while all other parameters are held constant. The numerical model is calibrated not only to

reproduce peak loads but also to capture the progressive, top-down debonding mechanism observed experimentally, interpreted as zipper-type interfacial propagation. Within this framework, the novelty of the present study lies not only in the adoption of sacrificial interface layers with CDP and element deletion, but also in transferring and reformulating this strategy for a fundamentally different composite system, namely concrete repair interfaces, and in establishing a unified experimental–numerical route that links a measurable repair mix variable, namely cement content, to the constitutive parameters governing interface failure. Based on a systematic parametric study, mix-dependent calibration curves are derived that relate cement content directly to shear bond strength (τ_b) and interface compressive strength (f_c^{int}), providing a practical, design-oriented tool for defining physically consistent interface parameters in FE models without resorting to iterative, case-specific numerical tuning.

2. Methodology

This paper presents a unified approach to predict the shear bond behavior at concrete repair interfaces through integration of a controlled experimental program with a calibrated finite element framework. The overall methodology is structured to ensure that material level mix design variables can be directly linked to the constitutive parameters required for numerical simulation. The methodology is organized into three complementary stages, whose integration and the transfer of information between the experimental and numerical domains are schematically summarized in Fig. 1.

(i) Experimental characterization. A shear push-out test series was conducted on composite specimens in which only the cement content of the repair mix was varied. Such a testing scheme ensures that the cement content is isolated as the major variable and all other parameters remain the same. Compressive strength tests were also carried out to characterize the mechanical properties of both substrate and repair concretes and to confirm the strength hierarchy required to force failure at the interface.

(ii) Numerical modeling and calibration. A three-dimensional finite element model was developed by adopting the concrete damaged plasticity combining with the sacrificial interface layers that is controlled by element deletion. The model has been calibrated against the experimental force-displacement curves as well as observed mechanisms of failure, ensuring that the zipper-type interfacial debonding can be reproduced in high fidelity. Interface compressive strength was then performed based on a parametric study, offering numerical bond strengths within the entire range of experiments.

(iii) Development of unified calibration curves. By combining the experimental measurements of shear bond strength with the numerically calibrated interface parameters, power law correlations were derived that directly relate repair cement content to both shear bond capacity and interface compressive strength. These correlations are a design-oriented tool that allows the selection of model parameters for a prescribed mix proportion in the absence of new numerical sensitivity analyses.

This methodological framework ensures consistency between material design, experimental benchmarking, and numerical simulation and provides a way in which the proposed calibration curves could practically act as a bridge between laboratory

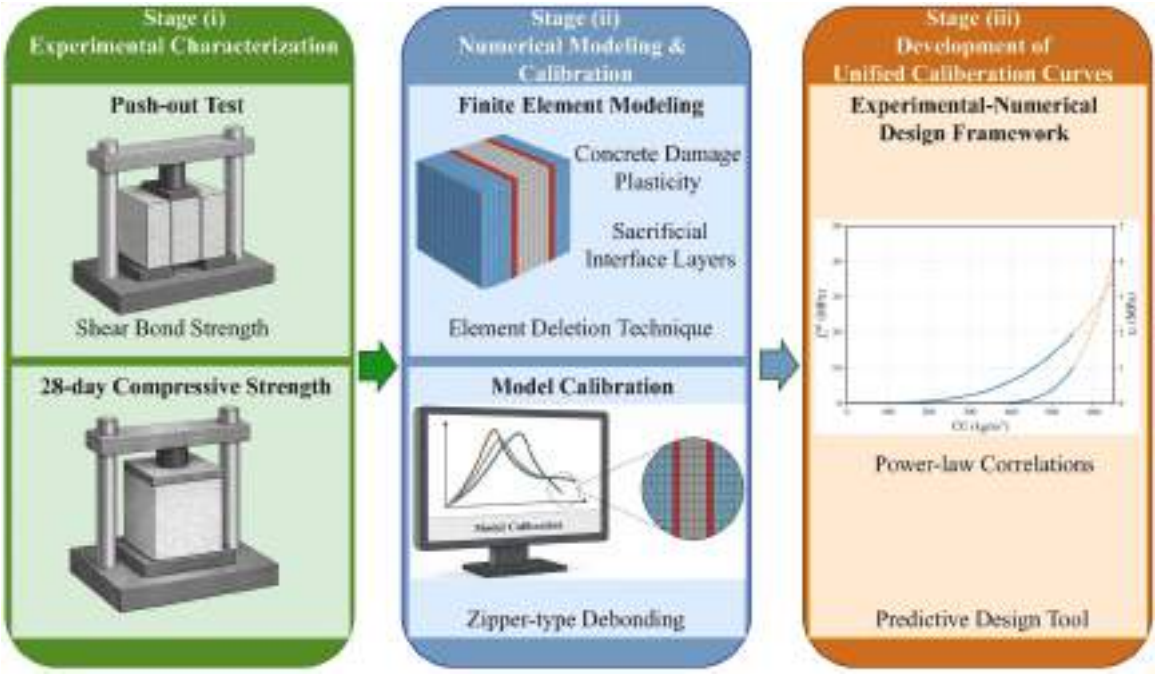

Fig. 1. Schematic flowchart of the integrated experimental and numerical methodology.

characterization and finite element modeling.

3. Experimental program

The experiments were designed to provide a benchmark to calibrate and validate the numerical model of the bond between a repair layer and a substrate concrete. Composite specimens were fabricated by casting a repair layer between two substrate blocks and tested in shear-splitting (push-out style) to quantify bond performance as a function of cement content in the repair concrete, with all other mix parameters held constant. This controlled variation of cement content allowed the direct isolation of its influence on interfacial behavior. Companion compressive strength tests were performed on the substrate and on each repair mix to contextualize bond results.

3.1. Materials and mix design

All mixes used Ordinary Portland Cement CEM I 42.5. The physical and chemical properties of the cement used in this study are presented in Table 1. The fine aggregate (sand) was natural river sand (apparent specific gravity 2690 kg/m^3; 24-h water absorption 1.6%). The coarse aggregate (gravel) had a maximum size of 19 mm. Fig. 2 presents the grading curves of the fine and coarse aggregates used in the mixtures in accordance with ASTM C33 [36]. Normal tap water was used. A polycarboxylate-based superplasticizer was used in the substrate concrete at a dosage of 1% by cement mass.

To ensure that the push-out tests were governed by interfacial failure rather than substrate crushing or splitting, the substrate concrete was proportioned with a target compressive strength deliberately higher than that of any repair mix [12,22]. This approach minimized parasitic failure modes and ensured that the measured response represented interfacial performance. The mixture design, therefore, included a lower water-to-cement ratio and superplasticizer to achieve the desired strength margin.

The substrate mixture had a water-to-cement ratio of 0.40, equal mass fractions of coarse and fine aggregate [36], and a superplasticizer dosage of 1% of cement content. The substrate mixture incorporated superplasticizer to ensure adequate workability, whereas the repair mixtures were intentionally prepared without superplasticizer to isolate the effect of cement content. Fig. 3 presents the mass-based mix proportion per cubic meter.

Repair concrete mixes differed only in cement content (300–550 kg/m^3) while maintaining w/c = 0.50 and no superplasticizer. Table 2 summarizes these proportions. This variation enabled a direct relationship between cement content and bond performance to be identified.

3.2. Composite specimen fabrication

Each composite specimen was a 150 mm cube composed of two outer substrate slabs, each measuring 150 × 150 × 50 mm, and a central repair layer, producing two bonded interfaces. This configuration allowed shear transfer along the interfaces while limiting the likelihood of substrate failure. Therefore, the load transfer mechanism during shear-splitting (push-out) was governed by the interface rather than by substrate crushing.

(i) Cast 150 mm substrate cubes; consolidate by vibration; water-cure 28 days.
(ii) Saw each substrate cube into 50 mm-thick slabs.
(iii) Place two substrate slabs in the mold, leaving 50 mm gap for the repair layer; clean bonding faces to saturated-surface-dry (SSD) condition.
(iv) Pour the repair concrete into the central gap and consolidate by vibration.
(v) Demold and water-cure the composite cubes for 28 days.

This fabrication process ensured consistent interface conditions across all specimens. It is illustrated in Fig. 4.

3.3. Mechanical testing

Compressive strength was measured at 28 days of age on 150 mm cubes for the substrate and for each repair mix following ASTM C39/C39M. Reported values are the mean of three specimens per mix (see Fig. 5 for the test setup) [37].

Shear Bond was evaluated using a shear-splitting (push-out) configuration on the composite cubes [12,21,22]. The applied

Table 1
Physical properties and Chemical composition of the utilized cement.

Physical Properties								
Specific Gravity (gr/cm3)		**Bulk Unit Weight (gr/cm3)**		**Specific Surface Area (cm2/gr)**		**Autoclave Expansion (%)**		**Color**
3.15		1.40		2910		0.07		Gray
Chemical Composition (%)								
CaO	**SiO2**	**Al2O3**	**Fe2O3**	**MgO**	**K2O**	**Na2O**	**SO3**	**L.O.I**
62.85	21.32	4.81	3.83	1.48	0.69	0.47	2.32	2.04

L.O.I: Loss of Ignition.

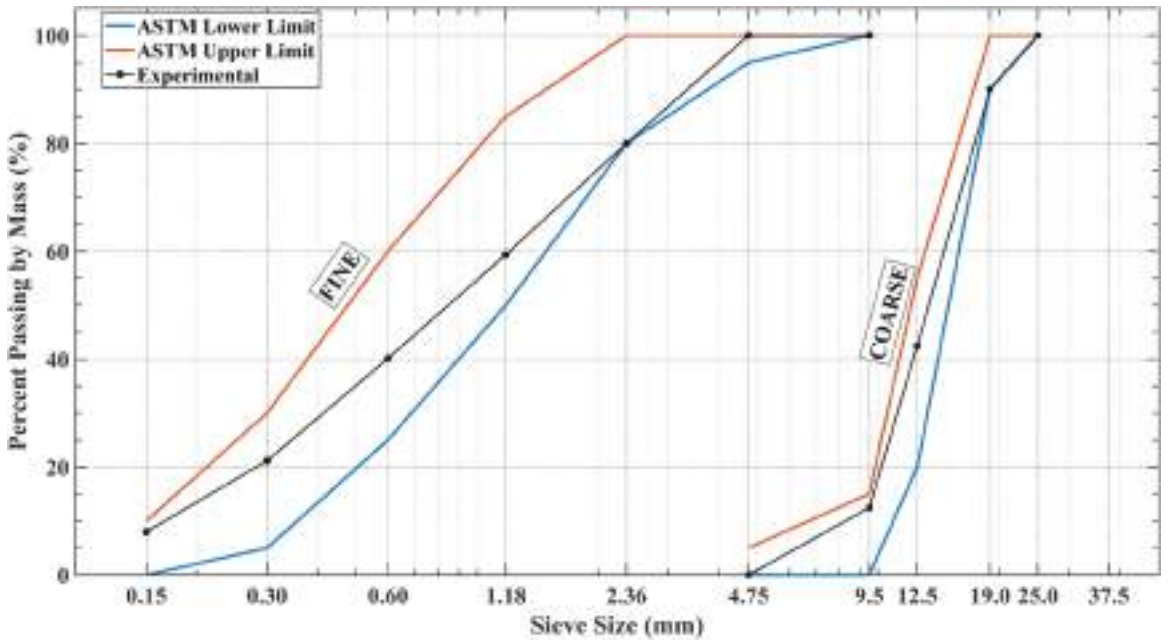

Fig. 2. Grading curves of the fine and coarse aggregates used in the mixtures.

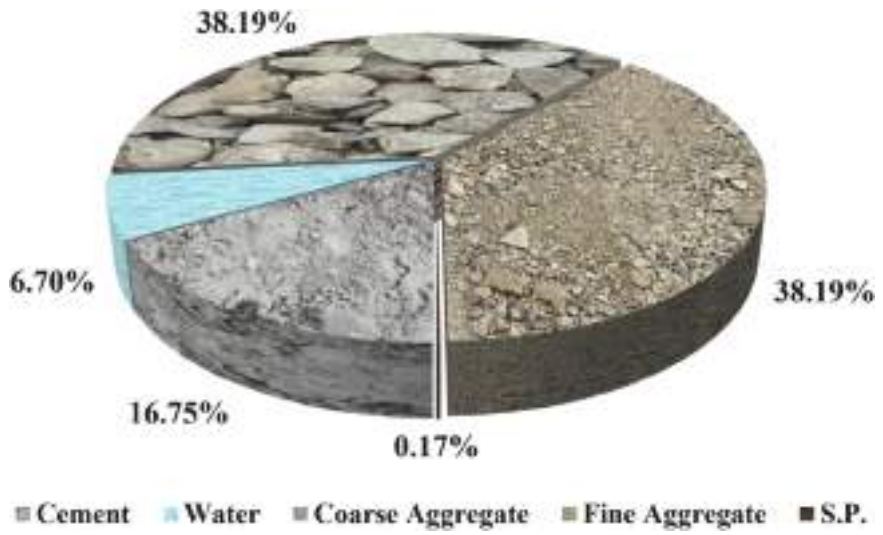

Fig. 3. Mass-based mix proportion of substrate concrete (per m^3).

Table 2
Mix proportions of repair concretes (per m^3).

Mix ID	Cement (kg/m^3)	Water (kg/m^3)	Fine Aggregate (kg/m^3)	Coarse Aggregate (kg/m^3)
R300	300	150	1003	1003
R350	350	175	919	919
R400	400	200	865	865
R450	450	225	811	811
R500	500	250	756	756
R550	550	275	702	702

Fig. 4. Fabrication process of composite specimens.

compression load mobilized shear along the two interfaces, while minimizing frictional contribution. The bond strength τ_b (MPa) was calculated according to Eq. (1):

$$\tau_b = \frac{F_{max}}{A_b} = \frac{F_{max}}{2A} \tag{1}$$

where F_{max} is the peak load recorded during the test (N), A_b is the total bonded area (mm^2), and A is the bonded area of a single interface. This method promoted failure strictly along the interfaces, providing a reliable measure of shear bond capacity.

Results are reported as the mean of three specimens per mix. The shear-splitting test configuration is illustrated in Fig. 5.

Table 3 summarizes the compressive strength of the substrate and repair concretes and the measured bond strength. Each reported value represents the average of three specimens, accompanied by its corresponding Coefficient of Variation (COV) to transparently indicate the range of experimental dispersion.

The experimental data served as a calibration and validation benchmark for the numerical model. By controlling all other mix parameters, the measured bond response was directly mapped to the interface-layer properties in the FE model.

4. Numerical modeling

The numerical modeling campaign was designed to reproduce the shear splitting response of the composite specimens under monotonic, displacement-controlled loading. The central objective was to validate a modeling strategy in which the bond region between substrate and repair concrete is represented explicitly by thin interface layers governed by Concrete Damaged Plasticity (CDP) with element deletion. This approach was designed to capture both (i) the peak reaction force and corresponding bond strength and (ii) the experimentally observed interface-localized failure pattern. All analyses were carried out in ABAQUS, using the same specimen geometry and loading configuration adopted in the experimental program (Fig. 6). The numerical response is evaluated primarily in terms of the global force–displacement curves and the evolution of damage and element deletion along the interface.

4.1. Model geometry

The finite-element model follows the composite configuration described in 3, using a 150 × 150 × 150 mm cube composed of two substrate regions and a central repair region. To resolve the bond zone explicitly, the central 50 mm of the specimen is subdivided into a 46 mm repair layer flanked by two thin interface layers, each 2 mm thick. Along the interface-normal direction, the sequence of

Fig. 5. Mechanical testing setups for compressive and shear-splitting tests.

Table 3
Compressive strength and bond strength.

Mix ID	Compressive Strength (f_c) (MPa)	COV (%)	Bond strength (τ_b) (MPa)	COV (%)
Substrate	36.29	7.30	-	
R300	23.5	5.34	0.21	1.18
R350	28.13	7.15	0.43	2.43
R400	30.79	4.12	0.67	5.11
R450	32.07	4.91	0.81	2.09
R500	31.92	3.11	1.53	1.73
R550	30.09	5.52	1.85	3.68

layers is therefore: Substrate (50 mm) – Interface (2 mm) – Repair (46 mm) – Interface (2 mm) – Substrate (50 mm).

The 2 mm interface layers were introduced as sacrificial bond zones, with mechanical properties selected such that cracking, damage, and eventual separation localize within them rather than in the adjacent concrete. The model domain is partitioned accordingly into five material regions, two substrates, two sacrificial interface layers, and one repair layer. This partitioning enforces nodal conformity across both interfaces, allowing shear transfer and debonding to be captured directly by the interface elements rather than through tied or contact constraints. Fig. 6 illustrates the composite specimen, the imposed displacement at the top surface, and the layer thicknesses used in the numerical model.

4.2. Mesh development and boundary conditions

A structured hexahedral mesh was adopted to capture interfacial damage with good numerical conditioning while keeping the model computationally efficient (Fig. 7). All solid regions, the two substrate blocks, the repair layer, and the sacrificial interface layers were discretized using eight-node linear brick elements with reduced integration (C3D8R). Mesh seeds were chosen so that the 2 mm interface layers were resolved using small, nearly cubic elements; at least two elements were placed through the interface thickness to resolve steep strain gradients and to ensure stable element deletion. To ensure the reliability of the element deletion technique and to mitigate potential mesh dependency issues associated with strain-based failure criteria, a preliminary mesh sensitivity analysis was conducted on the initial validation models. The adopted discretization (featuring approximately 1 mm elements within the sacrificial interface) was compared against a highly refined mesh utilizing 0.5 mm elements. The comparison yielded a negligible difference of

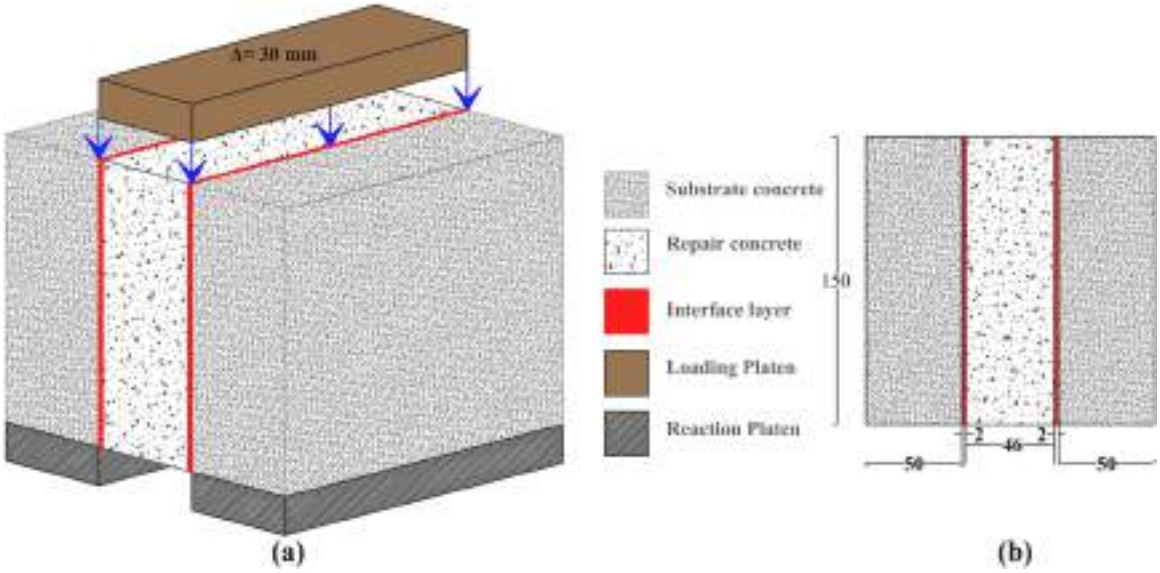

Fig. 6. Composite specimen: (a) displacement-controlled loading; (b) geometry and partitions with dimensions.

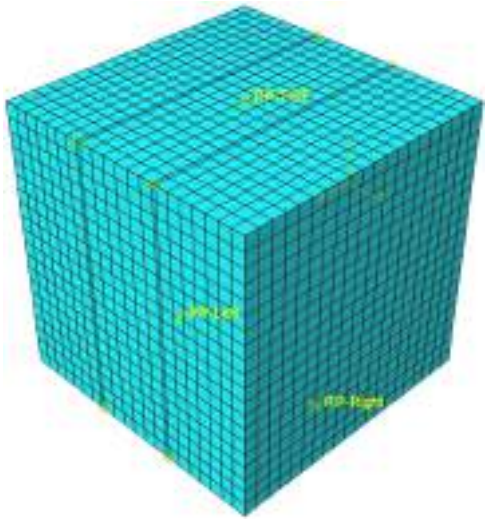

Fig. 7. Structured C3D8R mesh of the composite specimen with reference points (RPs).

less than 1% in the global force-displacement response and peak load predictions. Consequently, to balance stringent numerical accuracy with the substantial computational demands of the extensive parametric study, the 1 mm element size was deemed optimally converged and was maintained for all subsequent analyses. Away from the interfaces, a graded mesh was used to transition to coarser elements in the substrate and repair regions while maintaining acceptable aspect ratios and limiting hourglassing in C3D8R elements. No artificial stiffness, penalty contact, or mesh-dependent constraints were introduced in the interface layers.

Boundary conditions were defined to replicate the shear-splitting tests under displacement control. A reference point (RP_TOP) was created above the specimen, and a vertical displacement history with a total magnitude of 30 mm was prescribed at this point. The nodes on the top surface of the repair layer were kinematically coupled to RP_TOP, ensuring that only the repair region was directly loaded. The bottom surfaces of the two substrate layers were fully restrained in translation (U1 = U2 = U3 = 0), providing a reaction equivalent to the experimental setup, while the underside of the repair layer remained unloaded. Lateral faces were left traction-free to avoid artificial confinement. The displacement-time amplitude was calibrated such that the nominal stress rate, computed from the reaction force and loaded area, was approximately 0.14 MPa/s in accordance with ASTM C39/C39M [37]. The global reaction force was obtained by summing the nodal reactions on the restrained supports; its peak value, F_{max}, was subsequently used with Eq. (1) to compute the numerical bond strength. Fig. 7 shows the resulting structured mesh and the reference points employed for loading and monitoring.

4.3. Damage plasticity and failure

4.3.1. CDP model for substrate and repair parts

The substrate and repair parts were modeled using the CDP formulation available in ABAQUS, in order to reproduce non-linear behavior with stiffness degradation in both compression and tension. The input stress–strain curves and CDP parameters were defined on the basis of previously published calibration studies for normal-strength concrete, and their recommended parameter ranges for CDP [38,39], supplemented, where necessary, by the compressive stress–strain envelope proposed for reinforced concrete in compression [40,41]. Representative uniaxial stress–strain curves adopted in the model for the substrate concrete and all repair mixes are shown in Fig. 8, with compressive response on the left and tensile response on the right.

The stress–strain curves in Fig. 8 confirm that the CDP calibration reproduces both the intended strength hierarchy and the non-monotonic effect of cement content on mechanical response. In compression, the repair mixes show a clear increase in peak stress from R300 (23.5 MPa) through R350 and R400, with the maximum reached for R450 (32.07 MPa); R500 remains essentially at the same level as R450, while R550 (30.09 MPa) drops back to a value slightly below R400, indicating that cement contents beyond roughly 450 kg/m^3 no longer enhance, and may even impair, compressive strength. Although this reduction is modest (approximately 0.5% for R500 and 6% for R550 compared to the peak), it is a recognized physical consequence of mixture proportioning constraints. Because the water-to-cement ratio was maintained at a constant 0.50 across all repair mixtures, higher cement contents intrinsically necessitate a greater absolute volume of water in the mix. This elevated free water content significantly increases the mixture's susceptibility to drying shrinkage. The resulting volumetric contraction generates internal tensile stresses that induce micro-cracking within the bulk concrete matrix, ultimately impairing its macroscopic compressive capacity relative to the optimally proportioned R450 mix. The substrate curve forms the upper envelope of the responses, consistent with its role as a deliberately over-strength support in the shear-splitting tests. An analogous pattern appears in tension: the lowest tensile resistance is obtained for R300 (approximately 2.4 MPa), strengths rise for R350–R450, only marginally increase at R500, and then decline again at R550, whereas the substrate exhibits the highest tensile strength, about 3.5 MPa. Across all mixes, the post-peak branches in both compression and tension display similar gradual softening, with stresses decaying toward small residual values at large inelastic or cracking strains, so that the progressive degradation of stiffness implemented in CDP is consistent from one mix to another.

4.3.2. Sacrificial interface layer: parameters and thresholds

The bond region between the substrate and repair concretes was represented by two thin solid layers, each 2 mm thick, placed on either side of the repair layer. These layers were assigned CDP behavior and were treated as sacrificial zones in which damage is allowed to concentrate, and elements are permitted to fail, while the surrounding substrate and repair concretes remain stronger [35]. This strength hierarchy enforces localization of the shear-splitting failure in the numerical model at the same interface where debonding was observed in the experiments.

The mechanical parameter space explored for the interface material is summarized in Table 4. Thirteen interface cases were defined by combinations of interface compressive strength f_c^{int}, tensile strength f_t^{int} and Young's modulus E. The values were selected so that the resulting numerical bond strengths cover the practical interval for concrete–concrete interfaces and so that each experimental bond value can be matched by an appropriate interface case in the finite-element model. The corresponding constant CDP flow parameters for the interface material are listed in Table 5. These values were selected within ranges recommended in previous applications of CDP to concrete and bond/interface problems [35,42–45].

In the interface layers, the CDP response was expressed in the standard degraded-stiffness form. In tension, the nominal stress is given by

$$\sigma_t = (1 - d_t)\, E_0 \left(\varepsilon_t - \varepsilon_t^{pl}\right) \tag{2}$$

and in compression by

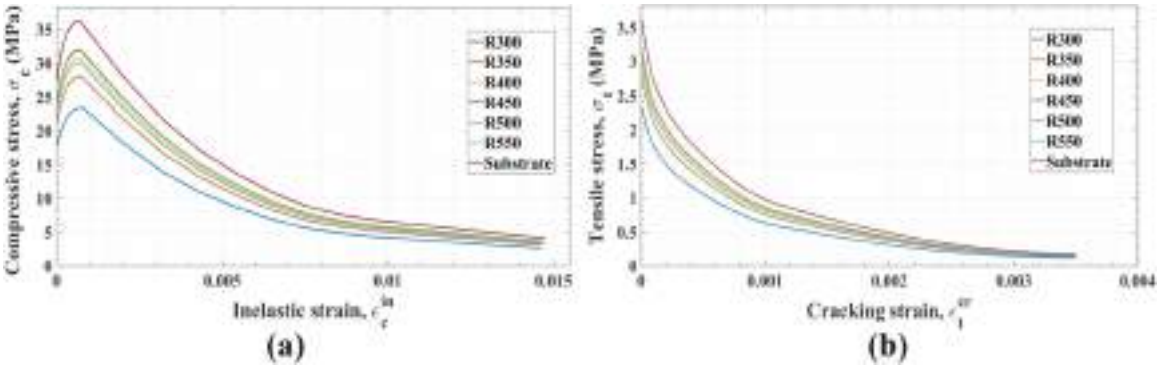

Fig. 8. Stress–strain curves used for CDP calibration: substrate and repair concretes; a) compression, b) tension.

Table 4
Interface layer: variable mechanical properties by case.

Interface Case ID	f_c^{int} (MPa)	f_t^{int}(MPa)	E (MPa)	Interface Case ID	f_c^{int} (MPa)	f_t^{int} (MPa)	E (MPa)
1	0.001	0.0001	158	8	3.500	0.3500	9 354
2	0.005	0.0005	354	9	5.000	0.5000	11 180
3	0.010	0.0010	500	10	7.500	0.7500	13 693
4	0.100	0.0100	1 581	11	10.000	1.0000	15 811
5	0.500	0.0500	3 536	12	15.000	1.5000	19 365
6	0.900	0.0900	4 743	13	20.000	2.0000	22 361
7	2.000	0.2000	7 071				

Table 5
CDP flow parameters.

ν	ψ	Eccentricity	f_{b0}/f_{c0}	K_c	Viscosity
0.2	38°	0.10	1.16	0.667	0.001

$$\sigma_c = (1 - d_c)\, E_0 \left(\varepsilon_c - \varepsilon_c^{pl}\right) \tag{3}$$

where E_0 Is the initial elastic modulus, $\varepsilon_t$and ε_c are the total tensile and compressive strains, $\varepsilon_t^{\mathrm{pl}}$ and $\varepsilon_c^{\mathrm{pl}}$ are the corresponding plastic (inelastic) strain components, and $d_t$and d_c are the tensile and compressive damage variables. Post-peak softening in the sacrificial layers is therefore governed by the evolution of the cracking strain in tension, $\varepsilon_t^{\mathrm{ck}}$, the inelastic strain in compression, $\varepsilon_c^{\mathrm{in}}$, and their associated damage variables $d_t(\varepsilon_t^{\mathrm{ck}})$ and $d_c(\varepsilon_c^{\mathrm{in}})$ [35,40,46].

For each interface case, these softening and damage curves were calibrated so that the global force–displacement response of the composite specimen and the localization of failure along the bond line were consistent with the corresponding experimental shear-splitting test. In practice, this required iterative adjustment of the critical cracking and inelastic strain levels that mark the onset of complete degradation in the interface elements. The final calibrated values of $\varepsilon_t^{\mathrm{ck}}$and $\varepsilon_c^{\mathrm{in}}$for all thirteen interface cases are reported in Table 6; they provide the strain criteria governing element deletion and the onset of progressive debonding in the sacrificial layers.

4.3.3. Element deletion and zipper-type debonding

Element deletion was activated in the interface layers to allow local bond failure and separation once a prescribed failure condition was reached. When this condition is satisfied, the affected elements lose their stiffness and are removed from the analysis, enabling the interface to open and slide while the surrounding substrate and repair concretes remain largely intact.

At each increment of the displacement-controlled analysis, ABAQUS evaluates the current total and inelastic/cracking strains in each interface element and updates the tensile and compressive damage variables, d_t and d_c, according to the CDP softening laws. The calibrated cracking and inelastic strain thresholds in Table 5 define the onset of complete degradation in the sacrificial layers. When, at an integration point, the damage in tension or compression reaches its critical value, and the associated cracking or inelastic strain exceeds the assigned threshold, the element is flagged as failed, and its contribution is removed from the global stiffness matrix. The load previously carried by that element is then redistributed to neighboring regions, which may in turn reach their own failure criteria as the imposed displacement increases [35,46,47].

The sequence of checks and updates used to implement this failure strategy is summarized in Fig. 9. After each global equilibrium step, the algorithm loops over the interface elements, updates damage and stiffness based on the current strain state, checks the failure criteria derived from Table 5, and either keeps the element active (with reduced stiffness) or deletes it. The analysis then proceeds to the next displacement increment, which captures both the peak reaction and the subsequent softening associated with progressive debonding.

The mechanical consequences of this strategy are illustrated schematically in Fig. 10 for the sacrificial interface layer. At low load levels, all elements across the 2 mm interface layer are intact and share the shear transfer between the repair and substrate concretes. As the imposed displacement increases, the shear and normal stresses within this sacrificial layer develop a strong gradient along the

Table 6
Calibrated strain thresholds for interface element deletion.

Interface Case ID	ε_t^{ck}	ε_c^{in}	Interface Case ID	ε_t^{ck}	ε_c^{in}
1	5.92e−05	1.558e−04	8	3.500e−03	9.211e−03
2	1.321e−04	3.477e−04	9	4.182e−03	1.101e−02
3	1.871e−04	4.924e−04	10	5.128e−03	1.349e−02
4	5.917e−04	1.557e−03	11	5.915e−03	1.557e−02
5	1.323e−03	3.481e−03	12	7.246e−03	1.907e−02
6	1.775e−03	4.669e−03	13	8.366e−03	2.202e−02
7	2.646e−03	6.964e−03			

```
Algorithm: The Element Deletion Workflow
 Initialize model
        - Define composite geometry
        - Define (2 mm) interface layers as sacrificial zones
        - Generate mesh (refined in interface layers)
        - Assign CDP material parameters
        - Apply boundary conditions and displacement-controlled loading
 for each time increment do
     Solve global equilibrium → get element stresses and strains
          for each interface element do
               Update CDP state variables from current strains
                    - cracking strain  ε_t^ck
                    - inelastic strain ε_c^in
                    - damage variables d_t , d_c
               Compute degraded stresses
                     σ_t = (1 − d_t) E_0 (ε_t − ε_t^pl)
                     σ_c = (1 − d_c) E_0 (ε_c − ε_c^pl)

                  if (d_t ≥ (d_t)_Threshold & ε_t^ck ≥ (ε_t^ck)_Threshold) or
                     (d_c ≥ (d_c)_Threshold & ε_c^in ≥ (ε_c^in)_Threshold)
                      then
                        // YES - Delete Element
                           → Mark element as failed (Set status = 0)
                           → Remove its stiffness contribution
                           → Allow load redistribution to neighboring elements
                        // debonding front advances along interface (zipper effect)
                  else
                        // NO - Element remains Active
                           → Keep element in mesh
                           → Stiffness is only reduced by current damage (d_t , d_c)
                        // no change in connectivity; carries load in next increments
                  end if
          end for
          Update global response for this increment
               - reaction force vs. imposed displacement
               - current crack/deleted-element pattern
          if stopping criterion is satisfied
               - target displacement reached or
               - reaction force dropped below threshold /full debonding observed)
              then
                // exit time-increment loop
                break
          end if
 end for
 Output final load-displacement curve and debonding pattern
```

Fig. 9. Algorithm for interface element deletion in the CDP model.

loading direction: elements in the portion of the interface closest to the applied displacement experience the highest demand and begin to accumulate damage. In the schematic these highly degraded but still active elements are shown in yellow; their stiffness has been significantly reduced by the CDP damage variables, yet they continue to transmit load. Once the combined damage–strain state in the most critical of these yellow elements reaches the calibrated failure threshold, they are deleted and represented in red, leaving a local gap in the sacrificial layer. Continued loading causes newly damaged (yellow) elements immediately ahead of the deleted zone to reach the failure criterion and convert to red, while damage spreads into the next row of intact elements. Consequently, a band of deleted elements propagates progressively along the sacrificial interface layer, followed by a fringe of severely damaged but still active elements. This sequential advance of a debonded strip behind an advancing damage front produces a progressive, end-initiated debonding pattern, akin to a zipper opening along the bond line, which is consistent with the experimentally observed crack path and generates a gradual, rather than abrupt, reduction in reaction force in the shear-splitting tests.

All simulations were run under displacement control in a quasi-static regime, with the prescribed displacement applied in a single

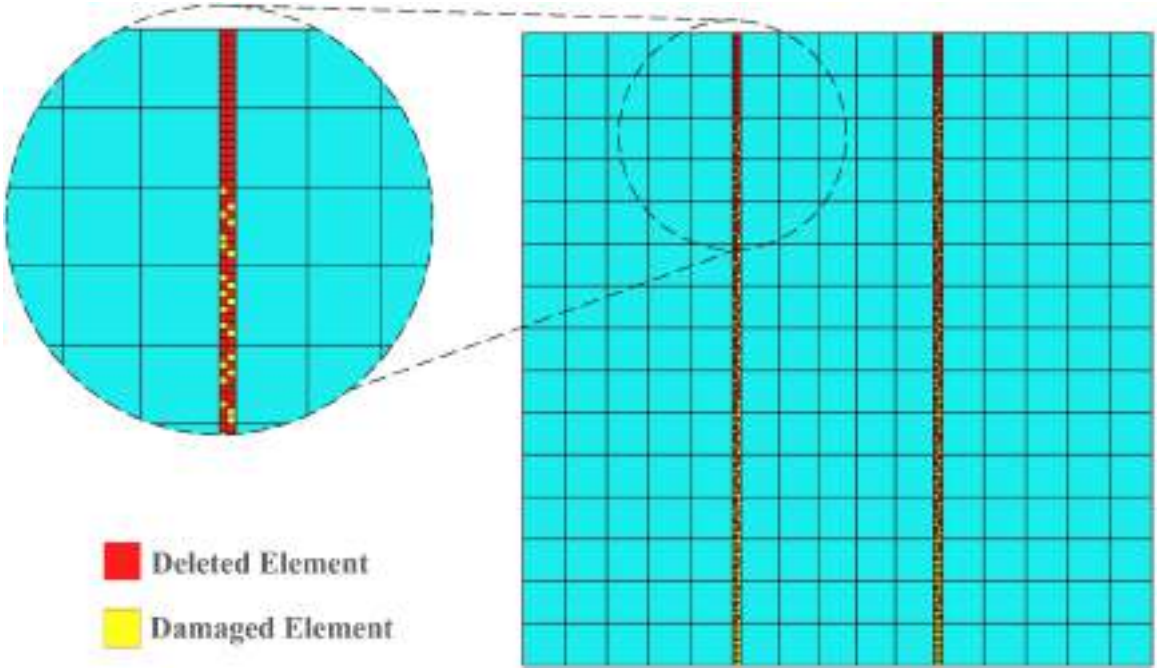

Fig. 10. Schematic of zipper-type debonding in the sacrificial interface layer.

analysis step. Numerical quasi-static conditions were checked by monitoring the global energy balance and keeping kinetic energy negligible compared with internal (strain) energy; no mass scaling was introduced. Post-peak response and interfacial separation were governed by the CDP softening behavior in the substrate, repair and sacrificial interface layers, together with the calibrated deletion thresholds assigned to the interface. The numerical output examined included the global reaction force–displacement response, the evolution of stress and strain fields, the development of tensile and compressive damage, and the spatial pattern of deleted elements interpreted as the crack path. These results form the basis for the comparisons and discussion presented in the next section.

5. Results and discussion

5.1. Stress distribution and debonding mechanism

The finite element model was used to analyze the progression of stress and damage in the composite specimen, with particular emphasis on the sacrificial 2 mm interface layers that control the onset of bond failure. An explicit dynamic solution scheme was adopted to simulate crack propagation, with the loading time extended sufficiently for the imposed displacement history to remain quasi-static and the loading rate to stay very low. This approach ensured numerical convergence while maintaining compatibility with the static nature of the laboratory tests. Fig. 11 illustrates, for the reference case with $f_c^{\text{int}} = 3.5\text{MPa}$, the full sequence of von Mises stress (σ_v) contours from the unloaded state to complete separation of the repair layer from the two substrate blocks. The results confirm that the simulated response is in close agreement with the experimental shear-splitting behavior.

At low load levels in Fig. 11, the contours show comparatively modest σ_v values within the substrate and repair blocks, while the sacrificial interfaces remain essentially elastic. As the imposed displacement increases, a concentrated band of elevated von Mises stress develops along the upper edge of each sacrificial interface, directly beneath the loaded face of the repair concrete. This band reflects the high local shear and normal stress combination required to trigger damage in the interface material. Once the local damage and strain thresholds are reached, the first interface elements at the top satisfy the deletion criterion and are removed from the mesh, creating a small debonded notch. With further loading, the region of high σ_v migrates progressively downwards along the 2 mm sacrificial layers on both sides of the repair block, and additional interface elements are deleted in sequence. The debonding front therefore advances step by step from the loaded edge towards the bottom of the specimen in a zipper-type, end-initiated debonding pattern, while the surrounding substrate and repair concrete remain largely intact. Just before complete detachment, the peak von Mises stress for this case reaches approximately 11.6 MPa in a narrow zone along the sacrificial band, whereas most of the cube remains in the green–cyan range, indicating that damage is strongly localized in the interface. This crack growth intensifies as loading increases until the sacrificial bands are entirely removed in the debonded region, and complete separation of the repair layer from the two substrate blocks is achieved. The correspondence between this simulated top-down debonding mechanism and the experimentally observed failure mode indicates that the numerical model reproduces both the failure path and the associated stress redistribution with good accuracy. In other words, the sacrificial layers successfully concentrate damage where physical evidence shows it to occur,

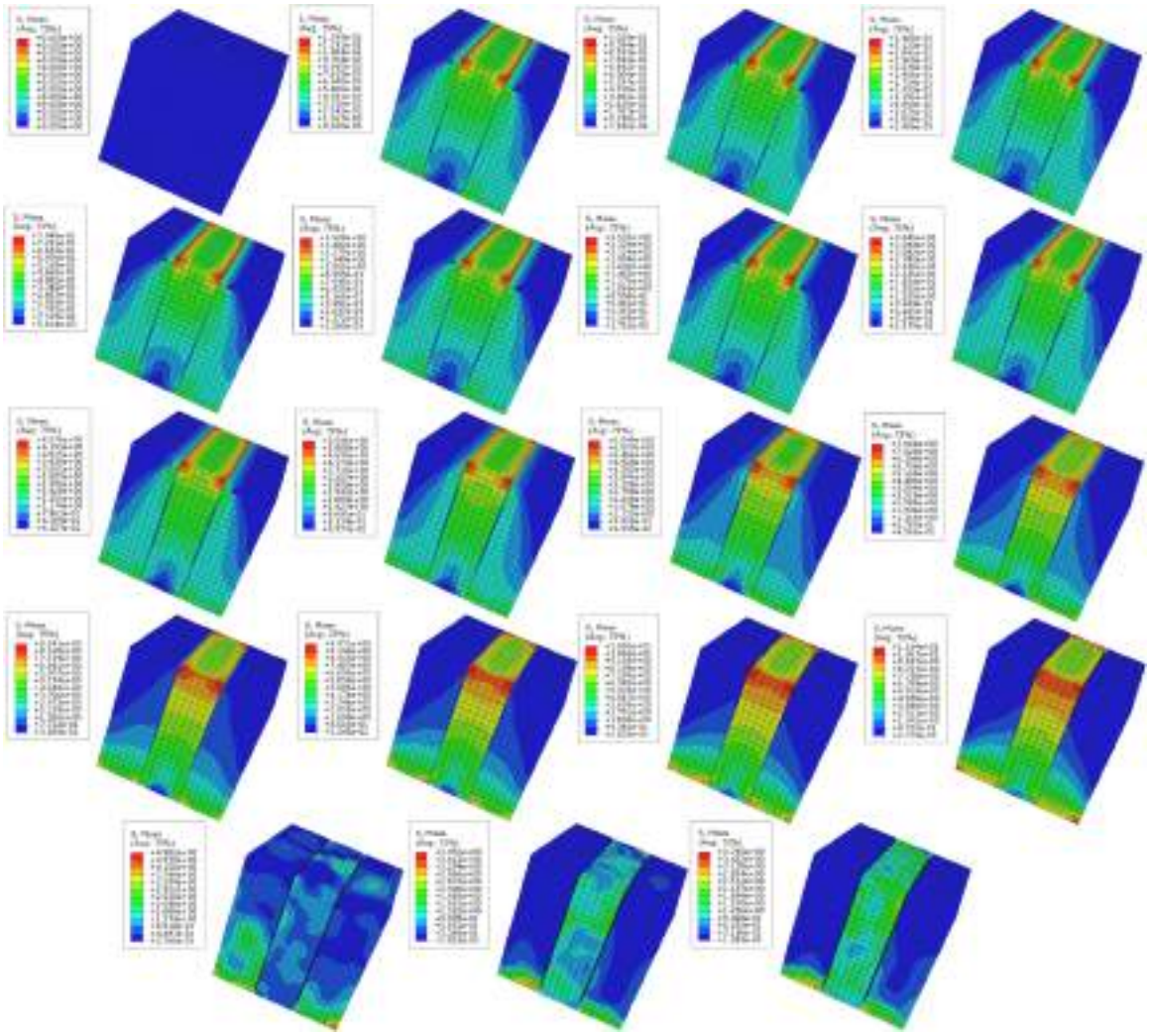

Fig. 11. Evolution of von Mises stress $\sigma_v$and debonding mechanism for the specimen with interface compressive strength $f_c^{\text{int}} = 3.5$MPa, showing top-down, zipper-type element deletion along the 2 mm sacrificial interfaces under shear-push-out loading.

supporting the physical soundness of the modeling strategy.

To complement this detailed sequence, the evolution of σ_v across the full range of f_c^{int} was condensed into a single dual-logarithmic envelope diagram (Fig. 12). For each interface case, defined by a f_c^{int} between 0.001 and 20 MPa, the smallest and largest von Mises stresses in the composite specimen were extracted from the final load step. These extrema, denoted $\sigma_{v,\min}$ and $\sigma_{v,\max}$, were then plotted as vertical color-graded bars on a dual logarithmic scale, with red circular markers indicating $\sigma_{v,\max}$ and blue square markers indicating $\sigma_{v,\min}$ for each f_c^{int}. Inset contour plots for three representative strengths ($f_c^{\text{int}} = 0.001$, 0.1 and 20 MPa) are superimposed on the diagram to show how the global stress levels in the specimen correspond to the local fields in very weak, intermediate, and strong interfaces.

The lower envelope $\sigma_{v,\min}$ remains of the order of few megapascals (10^{-5}MPa) for all interface strengths. For the weakest interface, the minimum von Mises stress in the composite is about 1.55×10^{-5}MPa at $f_c^{\text{int}} = 0.001$MPa (see Fig. 10), and it gradually increases to slightly higher values for stronger interfaces. This very small and weakly varying lower bound corresponds to regions that stay essentially elastic and only lightly stressed, for example remote corners of the cube away from the sacrificial bands. In contrast, the upper envelope $\sigma_{v,\max}$ shows a clear monotonic growth with increasing interface strength. For the most compliant interfaces the maximum von Mises stress is modest, about 2.13 MPa at $f_c^{\text{int}} = 0.001$ MPa, 3.24 MPa at 0.005 MPa, and 4.12 MPa at 0.01 MPa; in these cases, the sacrificial layers debond at very low stress levels and the global capacity is limited by early interface failure. As f_c^{int} increases, the interface can sustain higher stresses before the deletion criterion is reached, and $\sigma_{v,\max}$ rises to 6.50 MPa at 0.1 MPa, 8.58 MPa at 0.5 MPa, and 9.91 MPa at 0.9 MPa.

For intermediate and strong interfaces, the trend continues in a nearly proportional manner. When f_c^{int} is between 2 and 5 MPa, the

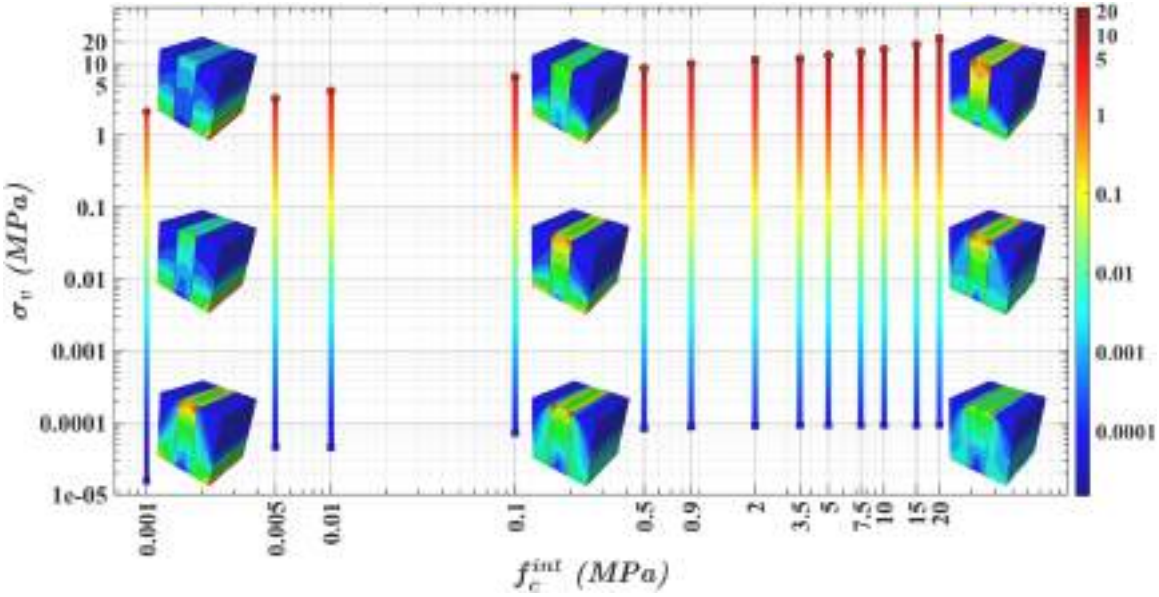

Fig. 12. Envelope of minimum and maximum σ_v bounds versus f_c^{int}, plotted on a dual logarithmic scale. The vertical gradient bars represent the stress span within the specimen, and the inset contours for $f_c^{\text{int}} = 0.001$, 0.1 and 20 MPa illustrate the associated stress fields at very weak, intermediate, and strong interfaces.

maximum von Mises stress grows from approximately 11.25 MPa (2 MPa) through 11.64 MPa (3.5 MPa) to 13.02 MPa (5 MPa). In this range, the sacrificial layer fails later in the loading process, and the stress field has more time to develop pronounced compressive struts through the substrate and repair blocks before debonding initiates. At higher interface strengths, the increase becomes more pronounced: $\sigma_{v,\max}$ reaches about 15.81 MPa at $f_c^{\text{int}} = 10$MPa, 18.39 MPa at 15 MPa, and finally 22.26 MPa at 20 MPa. These values confirm that a strong interface allows the composite specimen to mobilise a much larger portion of the inherent capacity of the substrate and repair concretes before the sacrificial band fails. The reference case $f_c^{\text{int}} = 3.5$MPa, for which the full stress evolution is shown in Fig. 11, sits near the middle of this envelope: its peak $\sigma_{v,\max}$ is high enough to mobilise significant compressive fields in both concretes, but still low enough that failure remains clearly governed by the sacrificial layer rather than by crushing in the bulk material.

The dual-logarithmic representation in Fig. 12 highlights two features consistent with the adopted element-deletion strategy. First, $\sigma_{v,\min}$ stays several orders of magnitude lower than $\sigma_{v,\max}$ for all f_c^{int}, which shows that damage and deletion remain concentrated in a narrow sacrificial zone rather than spreading through the entire body. Second, the smooth increase of $\sigma_{v,\max}$ with f_c^{int} reflects the transition from very brittle, early debonding at weak interfaces to a more progressive, zipper-type debonding pattern at stronger interfaces, in which the deletion front advances stepwise along the sacrificial layer before complete separation occurs. For low f_c^{int}, the interface elements satisfy the failure criterion soon after the first red zone appears near the top of the sacrificial layer; deletion occurs quickly, the von Mises peak remains low, and the reaction force drops sharply. For higher f_c^{int}, the same top-down mechanism operates,

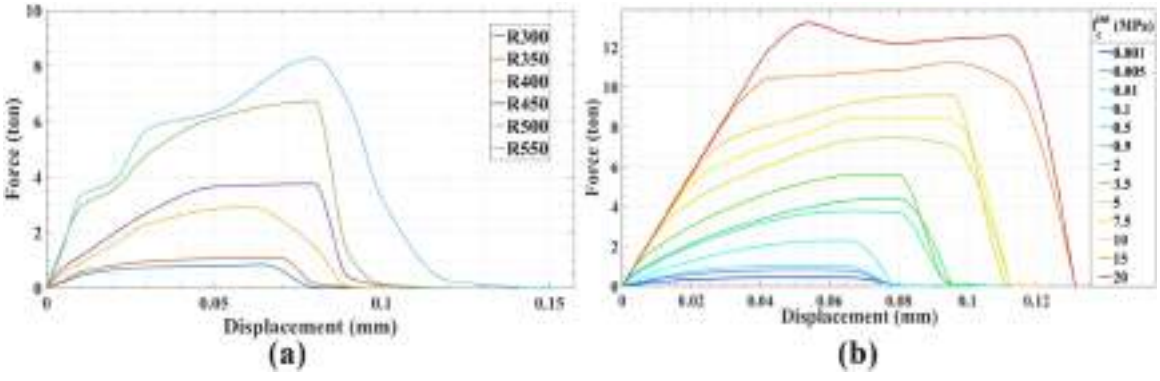

Fig. 13. Force–displacement response from shear bond push-out tests and numerical simulations: **a)** experimental curves for specimens with repair mortar cement contents R300–R550; **b)** FE simulations for varying f_c^{int} under the same loading configuration.

but the interface can accumulate higher stresses before the criterion is met, the deletion front travels further along the layer, and the global response exhibits a more extended post-peak tail. Figs. 11 and 12 provide a coherent picture of the stress distribution and debonding mechanism: the sacrificial interface strength f_c^{int} governs both the peak von Mises stress that the system can sustain and the extent of the progressive debonding process that precedes full detachment of the repair layer from the substrate.

This consistent behavior across the parametric study demonstrates that the proposed interface model is not only able to fit a single test, but also to reproduce the expected mechanical trends when the interface strength is varied systematically.

5.2. Force–displacement response

Fig. 13 compares the measured and simulated force–displacement responses of the shear bond push-out specimens. On the experimental side (Fig. 13a), increasing the cement content of the repair layer from R300 to R550 systematically enhances the global response. At very small displacements, the force–displacement curves are almost linear, indicating that shear transfer along the interface is initially governed by elastic mechanisms in the substrate, repair concrete, and interface. The peak force rises from well below 1 ton for R300 to about 8–9 ton for R550, while the associated displacement at peak increases from roughly 0.06–0.07 mm to nearly 0.10 mm, remaining confined to a relatively narrow range. This clustering of peak slips suggests that the onset of interfacial failure is controlled by localized microcracking and crushing in the vicinity of the sacrificial interface, rather than by large-scale sliding along the bond line. The initial slope of the curves also becomes steeper, indicating a stiffer composite as the repair mortar becomes denser and stronger. Post-peak, the low-cement mixes (R300, R350) exhibit a very sharp drop in load, characteristic of a brittle debonding of the sacrificial interface with limited energy dissipation. In contrast, mixes R450–R550 develop a broader plateau and a more gradual softening branch before complete loss of load, so that the area under the force–displacement curves (a proxy for energy dissipation) increases noticeably with cement content. This combination of rising peak force, modest variation in peak displacement, and growing energy dissipation establishes a clear interfacial performance hierarchy among R300–R550. This trend is consistent with broader observations in the concrete-repair literature, where the mechanical response of the interface has been shown to depend not only on surface condition and test configuration, but also on the mechanical compatibility and composition of the repair material [15, 19,20,25]. In the present study, because surface preparation, geometry, curing regime, and water-to-cement ratio were controlled, the observed increase in peak load and energy dissipation can be attributed primarily to the increase in repair cement content and the resulting change in the local interface-governing material response. Mechanistically, the richer cementitious matrix appears to have delayed the onset of unstable interfacial cracking and enabled a more progressive zipper-type debonding process, rather than an abrupt brittle loss of shear transfer. This also explains why the force–displacement curves evolved not only in peak magnitude, but also in post-peak shape, indicating that the interface response was governed by both strength and damage-propagation characteristics. In summary, the experiments reveal that higher cement content leads to a stiff, stronger, and more ductile interface response in shear.

It is crucial to highlight the distinct physical mechanisms governing bulk versus interfacial behavior, particularly for the high-cement mixtures. As observed in Table 3, while the bulk compressive strength experiences a slight reduction from R450 to R550, the interface shear strength more than doubles. This divergence indicates that macroscopic compressive strength is not the primary determinant of interfacial adhesion. Instead, the critical parameter is the total paste volume. Because the water-to-cement ratio was held constant, the R550 mixture contains a significantly higher volume of cement paste. While this excess paste increases drying shrinkage and causes minor strength degradation internally within the bulk matrix (as discussed in 4.3.1), it provides a substantial advantage at the boundary. The abundant paste facilitates much deeper penetration into the surface roughness of the substrate, drastically enhancing mechanical interlocking and interfacial adhesion. Although there is a physical limit where excessive paste-induced shrinkage would eventually impair the bond, within the evaluated range (up to 550 kg/m3), the benefits of paste-driven interlocking dominate the shear capacity. This physical mechanism confirms that the exponential growth captured by the subsequent calibration curves reflects actual Interfacial Transition Zone densification rather than a pure mathematical regression.

The numerical curves in Fig. 13b reproduce the same qualitative features when the compressive strength of the sacrificial interface, f_c^{int}, is varied from 0.001 to 20 MPa while keeping the substrate and repair concretes unchanged. Similar to the tests, the initial branches are almost linear, reflecting elastic shear transfer through the composite before damage initiates in the sacrificial band. For very weak interfaces ($f_c^{\text{int}} \leq 0.01$ MPa), the response is almost triangular: the load increases nearly linearly to a modest peak of about 0.3–1 ton, followed by an abrupt drop as element deletion is triggered in the sacrificial layer soon after the first local von Mises peak forms at the loaded edge. As f_c^{int} increases into the intermediate range (0.1–5 MPa), the curves broaden and the peak force rises to approximately 6–7 ton, with a more rounded maximum and a short softening branch. This behavior reflects the zipper-type, end-initiated debonding pattern identified in the previous subsection: interface elements at the top of the 2 mm layer delete sequentially rather than simultaneously, allowing the composite to carry load over a slightly larger displacement interval. For the strongest interfaces ($f_c^{\text{int}} \geq 10$ MPa), the model mobilises peak forces on the order of 10–15 ton with a pronounced plateau region, and the numerical curves show a substantial post-peak tail, indicating that the sacrificial interface can sustain progressive damage and dissipate significant fracture energy before complete separation.

A comparison of the two panels demonstrates that the finite-element model, with its sacrificial interface and element-deletion strategy, captures both the magnitude and shape of the experimental push-out responses in a physically consistent way. Weak numerical interfaces ($f_c^{\text{int}} \approx 0.001$–$0.1$ MPa) produce short, brittle curves similar in form to the R300–R350 tests, where debonding occurs almost immediately after the peak. Intermediate interface strengths ($f_c^{\text{int}} \approx 2$–$5$ MPa) generate peak forces and softening branches comparable to the R400–R450 specimens, while the strongest interfaces ($f_c^{\text{int}} \approx 10$–$20$ MPa) match the order of magnitude and plateau-

type behaviour of the R500–R550 curves. In terms of peak load, peak displacement, and overall energy dissipation (area under the curves), the numerical series therefore reproduces the same trends as the experimental one, once the repair classes are mapped to appropriate f_c^{int} levels [48]. This alignment supports the interpretation that the global shear bond capacity in the tests is governed primarily by the sacrificial interface rather than by crushing of the substrate or repair concretes. It also confirms that the numerical framework developed in 3, combining the CDP-based concrete model with a sacrificial interface layer and progressive, zipper-type element deletion, provides a robust representation of the experimentally observed bond–debond transition under shear push-out loading.

To move beyond qualitative visual assessment and rigorously validate the numerical framework, a quantitative error analysis was performed. To comprehensively evaluate the model across the tested spectrum, three representative experimental mixtures were strategically selected for numerical validation: R300, R400, and R550. These three cases effectively represent the lower limit, the intermediate transition, and the upper limit of the tested cohesive strengths. Three critical structural parameters were extracted from both the experimental and numerical force-displacement responses: Peak Load capacity, Slip at Peak Load, and total Energy Absorption. Table 7 details these comparative metrics. While perfectly replicating chaotic physical micro-cracking is theoretically unfeasible in macro-scale models, the calculated relative errors demonstrate that the numerical simulations successfully capture the structural hierarchy and energy dissipation mechanisms. The deviations remain well within the standard acceptable thresholds for highly non-linear explicit concrete damage mechanics, confirming the overall fidelity of the modeling strategy across all material regimes.

The reasonable quantitative agreement established in Table 7 is therefore not merely a visual correlation, but strong evidence that the proposed failure mechanism and interface modeling hypotheses are mechanically sound.

The ability of the proposed model to reproduce the interfacial slip prior to peak load, followed by progressive softening and energy dissipation, highlights an important advantage over conventional interface-modeling strategies. Simplified tie constraints [8,30], by enforcing perfect kinematic compatibility, would suppress relative slip and would therefore be unable to reproduce the experimentally observed post-peak softening branches shown in Fig. 13, leading to overestimation of composite action and bond capacity. Cohesive zone models can, in principle, simulate progressive debonding, but they generally rely on traction-separation or fracture-energy parameters [31–33] that are difficult to identify directly for repair systems with continuously varying cement contents, such as the 300–550 kg/m^3 range investigated herein. In contrast, the present approach captures the governing failure mechanism through the progressive downward migration of highly localized stress concentrations within the sacrificial interface layers, followed by sequential element deletion and zipper-type debonding. This enables the model to reproduce the experimentally observed crack propagation and post-peak response using a calibrated macroscopic interface parameter rather than iterative micro-parameter identification. From this perspective, the proposed framework provides not only a mechanically consistent representation of progressive bond failure, but also a more practical route for repair-oriented FE calibration.

5.3. Calibration of interface parameters as a function of cement content

The final step of the study was to link the macroscopic bond capacity observed in the shear push-out tests to the micromechanical parameters of the sacrificial interface layer used in the FE model. To this end, a two-stage calibration was carried out. First, the FE parametric study on the sacrificial interface layer provided, for each prescribed interface compressive strength f_c^{int}, the corresponding peak bond stress τ_b at which element deletion propagated through the 2-mm interface band. These purely numerical pairs $(f_c^{\text{int}}, \tau_b)$ are summarized in Table 8 and represent the backbone of the interface calibration. In all cases, the substrate concrete was cast and modelled with a much higher strength than the repair layer so that failure is forced to occur in the repair concrete and at the sacrificial interface, rather than in the substrate; f_c^{int} therefore acts as a numerical parameter that controls the onset of the experimentally observed debonding mechanism.

In a second step, the experimental peak bond stresses $\tau_{b,\text{exp}}$ from the push-out tests (defined in Eq. (1) as the maximum recorded force divided by the nominal bonded area) were substituted into the numerical f_c^{int}–τ_b calibration, which yielded, for each repair mix R300–R550, a predicted interface compressive strength f_c^{int}compatible with the measured bond capacity. Each of these calibrated f_c^{int}values were then associated with the cement content $CC$of the corresponding repair mix, thereby generating a dataset (CC, f_c^{int}). By

Table 7
Quantitative validation of the representative boundary models against experimental results.

Mix ID	Parameter	Experimental	FE Model	Error (%)
R300	Peak Load (ton)	0.85	1.05	23.50
(Lower bound)	Slip at Peak Load (mm)	0.065	0.054	16.92
	Energy Absorption (ton.mm)	0.0496	0.0576	16.12
R400	Peak Load (ton)	2.93	3.76	28.32
(Middle state)	Slip at Peak Load (mm)	0.060	0.066	10.00
	Energy Absorption (ton.mm)	0.1638	0.2197	34.12
R550	Peak Load (ton)	8.30	7.45	10.24
(Upper bound)	Slip at Peak Load (mm)	0.080	0.080	0.00
	Energy absorption (ton.mm)	0.6030	0.6007	0.38

Table 8
Interface layer compressive strength and bond strength obtained from the finite-element model.

f_c^{int} (MPa)	0.001	0.005	0.01	0.1	0.5	0.9	2.0	3.5	5.0	7.5	10	15	20
τ_b (MPa)	0.1	0.18	0.23	0.51	0.84	0.98	1.25	1.49	1.66	1.88	2.14	2.50	2.94

combining this dataset with the experimental $(CC, \tau_{b,\exp})$pairs and eliminating the intermediate variable f_c^{int}, two power-law correlations were finally expressed directly as functions of the cement content.

From a broader perspective, this calibration step represents a key distinction between the present study and much of the previously reported interface literature. Earlier experimental studies have generally identified empirical relationships between repair-material characteristics, test conditions, and measured bond strength, whereas more recent reviews have mainly synthesized the governing mechanisms, test methods, and influencing factors affecting concrete-to-concrete bond behavior [15,20]. In parallel, numerical studies have shown that interface formulations often require parameter calibration from prior experiments or analytical identification procedures rather than from directly usable mixture variables [34]. In contrast, the present framework converts a measurable repair-design variable, namely cement content, into two quantities of immediate relevance for interface simulation: the experimentally observable shear bond strength and the numerically calibrated interface compressive strength. This gives the calibration curves a more direct physical meaning and supports their interpretation as a practical bridge between mixture proportioning, observed bond behavior, and FE parameter selection.

These correlations are plotted in Fig. 14, where the horizontal axis represents the cement content *CC*of the repair concrete, the left vertical axis the interface compressive strength f_c^{int}, and the right vertical axis the shear bond strength τ_b. Within the experimental range $CC = 300$–$550\ \text{kg/m}^3$, the best-fit expressions are:

$$\tau_b = 3.64 \times 10^{-10}\ CC^{3.55} \tag{4}$$

$$f_c^{\text{int}} = 2.04 \times 10^{-29}\ CC^{10.777} \tag{5}$$

Fig. 14 summarizes these correlations in a single chart. The horizontal axis reports the cement content of the repair concrete, *CC*, while the left vertical axis gives the interface compressive strength, f_c^{int} (blue scale), and the right vertical axis the shear bond strength, τ_b(red scale). Solid portions of the curves cover the experimental calibration interval $CC = 300$–$550\ \text{kg/m}^3$, whereas the dashed extensions represent predictions for mixtures outside this range. Two vertical dashed lines at $CC = 300$ and $550\ \text{kg/m}^3$ delineate the domain in which both correlations are directly supported by the push-out tests and FE calibration. Within this window, the chart thus shows a non-linear, power-law increase of both $f_c^{\text{int}}$and $\tau_b$with increasing *CC*, as given by Eqs. (4) and (5).

The exponents in Eqs. (4) and (5) highlight the different sensitivity of the two responses to changes in cement content. The more moderate exponent for τ_b(3.55) implies a gradual increase in shear bond capacity with *CC*; for example, within the tested interval, the red curve in Fig. 14 shows that increasing the cement content from 300 to 550 kg/m^3 raises the predicted τ_b from about 0.23 MPa to nearly 2.0 MPa, which is consistent with the experimental trend that higher-strength repair mortars mobilize higher interface shear capacity under the shear push-out configuration. The much steeper exponent for f_c^{int}(10.777) indicates that, within the calibrated FE model, relatively modest increases in cement content at the upper end of the range require substantial increases in the interface compressive-strength parameter to reproduce the experimentally observed growth in peak load. This behaviour reflects the role of f_c^{int} as a numerical trigger for element deletion in the sacrificial interface layer: once the substrate concrete is sufficiently strong to remain essentially elastic, additional cement primarily enhances the resistance of the repair layer and its interfaces, rather than altering the response of the substrate blocks.

To quantify the predictive quality of these correlations, the usual coefficient of determination R^2 was complemented by error metrics based on the experimental and calibrated reference values. For a set of *N*observations $y_i$and predictions $\hat{y}_i$, the coefficient of determination, and the normalised RMSE (NRMSE) are defined as

$$R^2 = 1 - \frac{\sum_{i=1}^{N} (\hat{y}_i - y_i)^2}{\sum_{i=1}^{N} (y_i - \bar{y})^2} \tag{6}$$

$$\text{NRMSE} = \frac{\sqrt{\frac{1}{N}\sum_{i=1}^{N} (\hat{y}_i - y_i)^2}}{y_{\max} - y_{\min}} \tag{7}$$

where $\bar{y}$ is the mean of the observed values and $y_{\max}, y_{\min}$ are the maximum and minimum observed values in the calibration set. When these indices are applied to Eqs. (4) and (5), the resulting values are summarized in Table 9.

For the τ_b–*CC* correlation in Eq. (4), an NRMSE of about 5.8% indicates that the fitted curve reproduces the measured shear bond capacities with an average prediction error of only a few per cent of the experimental variation, consistent with the relatively tight

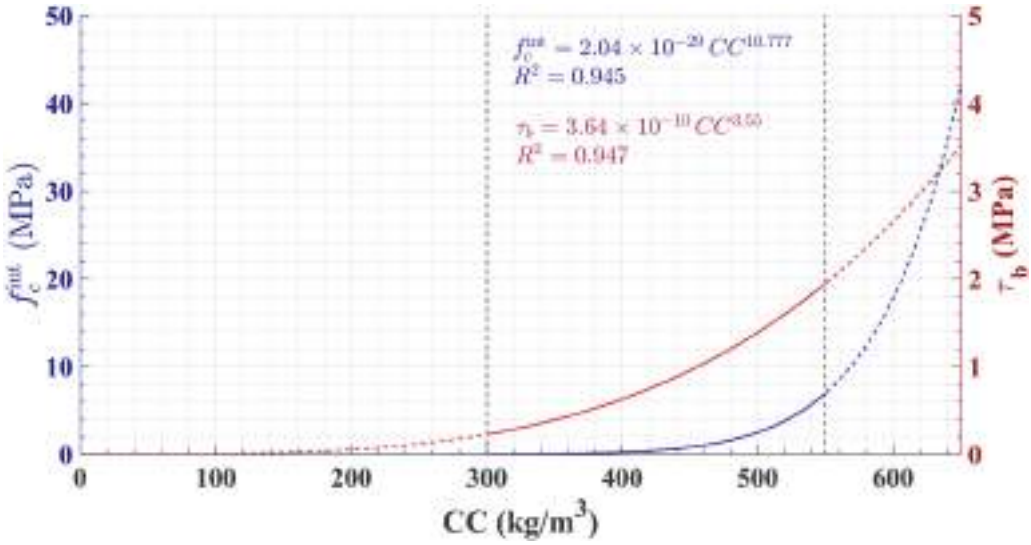

Fig. 14. Correlation of cement content of the repair concrete (*CC*) with (i) shear bond stress τ_b(red curve) and (ii) interface compressive strength f_c^{int}used for the sacrificial layer in the finite element model (blue curve). Dashed segments denote extrapolated portions; vertical dashed lines indicate the range of cement contents investigated experimentally (R300–R550).

Table 9
Statistical performance metrics for calibration curves.

Correlation	R^2	NRMSE (% of observed range)
τ_b–*CC* (Eq. 4)	0.947	5.8%
f_c^{int}–*CC* (Eq. 5)	0.945	8.7%

scatter typically reported for well-controlled push-out tests. For the f_c^{int}–*CC* correlation in Eq. (5), the NRMSE is approximately 8.7%, which is acceptable given that f_c^{int} is a calibrated modelling parameter for the sacrificial interface layer rather than a directly measured material strength. Taken together with the coefficients of determination $R^2_{\tau_b} = 0.947$ and $R^2_{f_c^{int}} = 0.945$, these values confirm that the power-law fits in Eqs. (4) and (5) provide a quantitatively reliable representation of both the experimental bond data and the calibrated interface strengths within the tested cement-content range, without being unduly influenced by the very small f_c^{int} values at the lower end of the calibration domain. In practical terms, this means that designers can use Fig. 14 and equivalent expressions as a simple tool to obtain consistent interface parameters for a given repair cement content, without repeating the entire experimental–numerical process.

The combined chart in Fig. 14, therefore, acts as a compact calibration tool rather than a purely empirical regression: for a given repair concrete with known cement content, Eq. (4) provides an estimate of the expected peak shear bond stress τ_b, while Eq. (5) yields a compatible value of $f_c^{int}$to be assigned to the sacrificial interface band so that the element-deletion process activates at the correct load level in the FE model. Conversely, if a target bond strength is specified, the same curves can be read in reverse to infer both a suitable cement content for the repair layer and an internally consistent interface strength parameter for CDP-based simulations. In this way, the calibration chart translates the combined experimental–numerical work into a compact design-oriented tool, embedding the sensitivity of the shear-bond response to repair strength while remaining consistent with the progressive, zipper-type debonding mechanism implemented in the numerical model. In this way, the calibration chart translates the combined experimental–numerical work into a compact design-oriented tool, embedding the sensitivity of the shear-bond response to repair strength while remaining consistent with the progressive, zipper-type debonding mechanism implemented in the numerical model.

It should be emphasized, however, that the reliability of Fig. 14 is highest within the cement-content interval actually covered by the tests and for repair systems similar to those investigated here (normal-strength cementitious overlays bonded to a prepared concrete substrate under quasi-static loading). Extrapolation of the curves to very low or very high cement contents, to mixtures with significant amounts of pozzolans, polymers, fibers, or to different substrate surface conditions and moisture states should be treated with caution, as these factors are known to strongly influence interface behavior and may alter the functional form of the correlations. Future work could extend the calibration framework by introducing additional axes or families of curves to account for other mix parameters (e.g., supplementary cementitious materials and fiber volume fraction) and substrate characteristics, and by refining the statistical basis of the fits with larger experimental datasets. Within its defined domain, however, the proposed chart offers a concise and quantitatively validated bridge between mix proportions, measured shear-bond performance, and the sacrificial interface

parameters required for predictive finite-element modelling. Consequently, the proposed calibration does not only fit the data, but also provides a structured way of embedding shear bond physics into CPD-based interface models.

Finally, although the calculated R^2 and NRMSE values indicate a strong correlation and low predictive error within the specific range of the present experimental program, the statistical limitation associated with the sample size must be acknowledged. Deriving continuous empirical relationships from only six discrete data points, even when these span the investigated range of repair mixtures, necessarily limits the broader statistical robustness of the proposed equations. Therefore, Eqs. (4) and (5) should be interpreted as a preliminary phenomenological framework valid within the investigated domain, rather than as universal design formulas. Establishing more generalized and statistically robust calibration relationships will require future studies based on a substantially larger database of experimental push-out tests covering a wider range of repair mixtures, interface conditions, and material parameters.

6. Conclusion

This study developed and validated a finite element framework based on Concrete Damaged Plasticity and 2 mm sacrificial interface layers with element deletion to simulate shear bond behavior at concrete repair interfaces. The numerical strategy was benchmarked against shear push-out tests performed on repair concretes with cement contents ranging from 300 to 550 kg/m^3 , using an over strength substrate to ensure that failure was confined to the repair substrate interface.

The experimental results showed a consistent interfacial response characterized by a stiff ascending branch, a distinct peak load, and pronounced post peak softening, with shear bond strength increasing from approximately 0.21 MPa to 1.85 MPa as cement content increased. The finite element simulations reproduced the measured force-displacement responses with satisfactory quantitative agreement. Quantitative validation of representative mixtures demonstrated that the model captures peak capacities and energy dissipation within acceptable error margins, with deviations below 29% despite the highly non-linear nature of the explicit fracture process. Furthermore, the model successfully captured the experimentally observed progressive, top-down zipper-type debonding mechanism localized within the sacrificial interface layers. This progressive failure is mechanically driven by highly localized interfacial shear stress concentrations that trigger sequential element deletion, accurately mirroring the physical crack propagation along the bond line.

A key outcome of the study is the derivation of mix-dependent calibration curves that directly link repair cement content to shear bond strength and interface compressive strength used in the finite element model. The resulting power law correlations achieved coefficients of determination close to 0.95 with normalized errors below 10%, providing a practical and design-oriented tool for defining physically consistent interface parameters without iterative numerical tuning.

Within its defined scope, the proposed framework offers a physically grounded bridge between mix proportioning and structural simulation, enabling predictive modeling of repair interface behavior using readily available material descriptors.

The study is subject to limitations related to the specific repair system and loading conditions investigated. The experimental and numerical analyses focused on normal strength cementitious overlays bonded to a single substrate type under monotonic quasi-static loading, and the calibration curves were derived for a limited range of cement contents.

Future research should extend the proposed methodology to different substrate conditions, alternative loading regimes, and more complex repair mixtures incorporating supplementary cementitious materials, polymers, or fibers.

CRediT authorship contribution statement

Majid Movahedi Rad: Writing – review & editing, Validation, Supervision, Resources, Methodology. **Marco Domaneschi:** Writing – review & editing, Validation, Investigation. **Oveys Ghodousian:** Writing – review & editing, Validation, Supervision, Software, Methodology, Data curation, Conceptualization. **Vahid Shafaie:** Writing – original draft, Visualization, Software, Resources, Investigation, Formal analysis, Data curation.

Funding

This research received no external funding.

Declaration of Competing Interest

The authors declare that they have no known competing financial interests or personal relationships that could have appeared to influence the work reported in this paper.

Acknowledgements

The authors would like to acknowledge the support of those who directly or indirectly contributed to the success of this study.

Data availability

Data will be made available on request.

References

[1] A.D. Espeche, J. León, Estimation of bond strength envelopes for old-to-new concrete interfaces based on a cylinder splitting test, Constr. Build. Mater. 25 (2011) 1222–1235, https://doi.org/10.1016/J.CONBUILDMAT.2010.09.032.

[2] D.R. Morgan, Compatibility of concrete repair materials and systems, Constr. Build. Mater. 10 (1996) 57–67, https://doi.org/10.1016/0950-0618(95)00060-7.

[3] B.A. Tayeh, B.H. Abu Bakar, M.A. Megat Johari, Y.L. Voo, Mechanical and permeability properties of the interface between normal concrete substrate and ultra high performance fiber concrete overlay, Constr. Build. Mater. 36 (2012) 538–548, https://doi.org/10.1016/j.conbuildmat.2012.06.013.

[4] K.L. Scrivener, A.K. Crumbie, P. Laugesen, The Interfacial Transition Zone (ITZ) between cement paste and aggregate in concrete, Interface Sci. 12 (2004) 411–421, https://doi.org/10.1023/B:INTS.0000042339.92990.4c.

[5] M.A. Al-Osta, S. Ahmad, M.K. Al-Madani, H.R. Khalid, M. Al-Huri, A. Al-Fakih, Performance of bond strength between ultra-high-performance concrete and concrete substrates (concrete screed and self-compacted concrete): an experimental study, J. Build. Eng. 51 (2022) 104291, https://doi.org/10.1016/J.JOBE.2022.104291.

[6] P.H. Emmons, A.M. Vaysburd, System concept in design and construction of durable concrete repairs, Constr. Build. Mater. 10 (1996) 69–75, https://doi.org/10.1016/0950-0618(95)00065-8.

[7] M. Naderi, O. Ghodousian, Adhesion of self-compacting overlays applied to different concrete substrates and its prediction by fuzzy logic, J. Adhes. 88 (2012) 848–865, https://doi.org/10.1080/00218464.2012.705673.

[8] E.N.B.S. Júlio, F.A.B. Branco, V.D. Silva, J.F. Lourenço, Influence of added concrete compressive strength on adhesion to an existing concrete substrate, Build. Environ. 41 (2006) 1934–1939, https://doi.org/10.1016/j.buildenv.2005.06.023.

[9] S. Feng, H. Xiao, J. Geng, Bond strength between concrete substrate and repair mortar: effect of fibre stiffness and substrate surface roughness, Cem. Concr. Compos 114 (2020) 103746, https://doi.org/10.1016/j.cemconcomp.2020.103746.

[10] D.P. Bentz, I. De la Varga, J.F. Muñoz, R.P. Spragg, B.A. Graybeal, D.S. Hussey, D.L. Jacobson, S.Z. Jones, J.M. LaManna, Influence of substrate moisture state and roughness on interface microstructure and bond strength: slant shear vs. pull-off testing, Cem. Concr. Compos 87 (2018) 63–72, https://doi.org/10.1016/j.cemconcomp.2017.12.005.

[11] P.M.D. Santos, E.N.B.S. Júlio, Factors affecting bond between new and old concrete, Acids Mater. J. 108 (2011) 449–456. ⟨https://api.semanticscholar.org/CorpusID:137674943⟩.

[12] V. Shafaie, O. Ghodousian, A. Ghodousian, R. Cucuzza, M. Movahedi Rad, Integrating push-out test validation and fuzzy logic for bond strength study of fiber-reinforced self-compacting concrete, Constr. Build. Mater. 425 (2024), https://doi.org/10.1016/j.conbuildmat.2024.136062.

[13] V. Shafaie, O. Ghodousian, A. Ghodousian, M. Gorji, H. Mehdikhani, M. Movahedi Rad, Shear bond strength in stone-clad façades: effect of polypropylene fibers, curing, and mechanical anchorage, Polymers 16 (2024), https://doi.org/10.3390/polym16212975.

[14] C. Zanotti, P.H.R. Borges, A. Bhutta, N. Banthia, Bond strength between concrete substrate and metakaolin geopolymer repair mortar: effect of curing regime and PVA fiber reinforcement, Cem. Concr. Compos 80 (2017) 307–316, https://doi.org/10.1016/j.cemconcomp.2016.12.014.

[15] A. Momayez, M.R. Ehsani, A.A. Ramezanianpour, H. Rajaie, Comparison of methods for evaluating bond strength between concrete substrate and repair materials, Cem. Concr. Res. 35 (2005) 748–757, https://doi.org/10.1016/J.CEMCONRES.2004.05.027.

[16] M. Lukovic, G. Ye, K. Van Breugel, Reliable concrete repair: A critical review, 14th Int. Conf. Struct. Faults Repair, Edinburgh, Scotland, UK, 3-5 July 2012 (2012). ⟨https://repository.tudelft.nl/islandora/object/uuid:0bb2bee0-027c-4384-a1fc-c995c9bba1c0⟩.

[17] K. Gadri, A. Guettala, Evaluation of bond strength between sand concrete as new repair material and ordinary concrete substrate (The surface roughness effect), Constr. Build. Mater. 157 (2017) 1133–1144, https://doi.org/10.1016/j.conbuildmat.2017.09.183.

[18] S. Zuo, J. Xiao, Q. Yuan, Comparative study on the new-old mortar interface deterioration after wet-dry cycles and heat-cool cycles, Constr. Build. Mater. 244 (2020) 118374, https://doi.org/10.1016/J.CONBUILDMAT.2020.118374.

[19] H. Liu, H. Zou, J. Zhang, J. Zhang, Y. Tang, J. Zhang, Y. Guo, J. Xiao, Interface bonding properties of new and old concrete: a review, Front. Mater. 11 (2024). ⟨https://www.frontiersin.org/journals/materials/articles/10.3389/fmats.2024.1389785⟩.

[20] D. Daneshvar, A. Behnood, A. Robisson, Interfacial bond in concrete-to-concrete composites: a review, Constr. Build. Mater. 359 (2022) 129195, https://doi.org/10.1016/j.conbuildmat.2022.129195.

[21] O. Ghodousian, R. Garcia, V. Shafaie, A. Ghodousian, Interfacial bond strength of coloured SCC repair layers: an experimental and optimisation study, J. Struct. Integr. Maint. 8 (2023) 140–149, https://doi.org/10.1080/24705314.2023.2170620.

[22] V. Shafaie, O. Ghodousian, A. Ghodousian, M. Homayounfar, M. Movahedi Rad, Slant shear tests and fuzzy logic integration for evaluating shear bond strength in SCC and FRSCC repair applications, Case Stud. Constr. Mater. 22 (2025) e04176, https://doi.org/10.1016/j.cscm.2024.e04176.

[23] C. Zanotti, N. Randl, Are concrete-concrete bond tests comparable? Cem. Concr. Compos 99 (2019) 80–88, https://doi.org/10.1016/j.cemconcomp.2019.02.012.

[24] O. Ghodousian, A. Ghodousian, V. Shafaie, S. Hajiloo, M. Movahedi Rad, Study of bonding between façade stones and substrates with and without anchorage using shear-splitting test—case study: travertine, granite, and marble, Buildings 13 (2023), https://doi.org/10.3390/buildings13051229.

[25] S. Austin, P. Robins, Y. Pan, Shear bond testing of concrete repairs, Cem. Concr. Res. 29 (1999) 1067–1076, https://doi.org/10.1016/S0008-8846(99)00088-5.

[26] V. Shafaie, M. Movahedi Rad, Multi-objective genetic algorithm calibration of colored self-compacting concrete using DEM: an integrated parallel approach, Sci. Rep. 14 (2024) 1–16, https://doi.org/10.1038/s41598-024-54715-4.

[27] V. Shafaie, M. Movahedi Rad, Dem-driven investigation and AutoML-Enhanced prediction of Macroscopic behavior in cementitious composites with Variable frictional parameters, Mater. Des. 254 (2025) 114069, https://doi.org/10.1016/j.matdes.2025.114069.

[28] A. Monserrat-López, A. Nogales, A. de la Fuente, Experimental characterization of concrete-to-concrete interface shear strength design-oriented constitutive parameters, Structures 55 (2023) 1172–1185, https://doi.org/10.1016/j.istruc.2023.06.075.

[29] M.E. El Dandachy, D. AlMohamad, M. Briffaut, A. El-Mir, J.J. Assaad, H. El-Hassan, Assessment of concrete-to-concrete shear bond behavior using 3-D direct shear testing, Results Eng. 24 (2024) 103000, https://doi.org/10.1016/j.rineng.2024.103000.

[30] M. Farzad, M. Shafieifar, A. Azizinamini, Experimental and numerical study on bond strength between conventional concrete and Ultra High-Performance Concrete (UHPC), Eng. Struct. 186 (2019) 297–305, https://doi.org/10.1016/j.engstruct.2019.02.030.

[31] F. Moroni, A. Pirondi, Cohesive zone model simulation of fatigue debonding along interfaces, Procedia Eng. 10 (2011) 1829–1834, https://doi.org/10.1016/j.proeng.2011.04.304.

[32] V. Savino, L. Lanzoni, A.M. Tarantino, M. Viviani, A cohesive model to predict the loading bond capacity of concrete structures repaired/reinforced with HPFRC/UHPFRC and stressed to mixed mode, Cem. Concr. Compos 112 (2020) 103673, https://doi.org/10.1016/j.cemconcomp.2020.103673.

[33] M. Elices, G.V. Guinea, J. Gómez, J. Planas, The cohesive zone model: advantages, limitations and challenges, Eng. Fract. Mech. 69 (2002) 137–163, https://doi.org/10.1016/S0013-7944(01)00083-2.

[34] X.-B. Luu, S.-K. Kim, Finite element modeling of interface behavior between normal concrete and ultra-high performance fiber-reinforced concrete, Buildings 13 (2023) 950, https://doi.org/10.3390/buildings13040950.

[35] F. Shahidi, V. Shafaie, O. Ghodousian, S.A. Emamian, M. Movahedi Rad, Numerical investigation of bonding in stone-clad Façades: comparative analysis with and without mechanical anchorage, J. Infrastruct. Preserv. Resil. 6 (2025) 36, https://doi.org/10.1186/s43065-025-00157-9.

[36] ASTM C33/C33M-18, Standard Specification for Concrete Aggregates, West Conshohocken, PA, 2018. https://doi.org/10.1520/C0033_C0033M-18.

[37] ASTM C39/C39M-23, Standard Test Method for Compressive Strength of Cylindrical Concrete Specimens, Am. Soc. Test. Mater, Pennsylvania, USA, 2023.

[38] B. Wahalathantri, D. Thambiratnam, T. Chan, S. Fawzia, A material model for flexural crack simulation in reinforced concrete elements using ABAQUS. Proc. First Int. Conf. Eng. Des. Dev. Built Environ. Sustain. Wellbeing, Queensland University of Technology, 2011, pp. 260–264.

[39] T. Jankowiak, T. Łodygowski, Identification of parameters of concrete damage plasticity constitutive model, Found. Civ. Environ. Eng. 6 (2005) 53–69. ⟨https://api.semanticscholar.org/CorpusID:136560789⟩.

[40] D.C. Kent, R. Park, Flexural members with confined concrete, J. Struct. Div. 97 (1971) 1969–1990, https://doi.org/10.1061/JSDEAG.0002957.

[41] R. Park, D. Kent, R. Sampson, Reinforced concrete members with cyclic loading, J. Struct. Div. (1972).
[42] M. Hanifehzadeh, B. Gencturk, R. Mousavi, A numerical study of spent nuclear fuel dry storage systems under extreme impact loading, Eng. Struct. 161 (2018) 68–81, https://doi.org/10.1016/J.ENGSTRUCT.2018.01.068.
[43] S. Aaleti, B. Petersen, S. Sritharan, Design Guide for Precast UHPC Waffle Deck Panel System, including Connections, 2013. ⟨https://www.researchgate.net/publication/284717870_Design_Guide_for_Precast_UHPC_Waffle_Deck_Panel_System_including_Connections⟩.
[44] M. Shafieifar, M. Farzad, A. Azizinamini, Experimental and numerical study on mechanical properties of Ultra High Performance Concrete (UHPC), Constr. Build. Mater. 156 (2017) 402–411, https://doi.org/10.1016/J.CONBUILDMAT.2017.08.170.
[45] M. Shafieifar, V. Khonsari, A Numerical Investigation on Behavior of Column Base Plates with Different Configurations, Civ. Eng. J. 4 (2018) 1223–1239, https://doi.org/10.28991/CEJ-0309169.
[46] ABAQUS, ABAQUS Theory Manual, Hibbitt, Karlsson & Sorensen, Incorporated, 2022.
[47] Marco Domaneschi, Experimental and numerical study of standard impact tests on polypropylene pipes with brittle behaviour, Proc. Inst. Mech. Eng. Part B J. Eng. Manuf. 226 (2012) 2035–2046, https://doi.org/10.1177/0954405412461983.
[48] A. Dey, D. Valiukas, R. Jakubovskis, A. Sokolov, G. Kaklauskas, Experimental and numerical investigation of bond-slip behavior of high-strength reinforced concrete at service load, Materials 15 (2022), https://doi.org/10.3390/ma15010293.